
AN AUTOENCODER COMPRESSION APPROACH FOR ACCELERATING LARGE-SCALE INVERSE PROBLEMS

A PREPRINT

Jonathan Wittmer

Oden Institute for Computational Science and Engineering
University of Texas at Austin
Austin, TX 78712
jonathan.wittmer@utexas.edu

Jacob Badger

Oden Institute for Computational Science and Engineering
University of Texas at Austin
Austin, TX 78712
jcbadger@utexas.edu

Hari Sundar

Department of Computer Science
University of Utah
Salt Lake City, Utah 84112
hari.sundar@utah.edu

Tan Bui-Thanh

Department of Aerospace Engineering and Engineering Mechanics
Oden Institute for Computational Science and Engineering
University of Texas at Austin
Austin, TX 78712
tanbui@oden.utexas.edu

April 12, 2023

ABSTRACT

PDE-constrained inverse problems are some of the most challenging and computationally demanding problems in computational science today. Fine meshes that are required to accurately compute the PDE solution introduce an enormous number of parameters and require large scale computing resources such as more processors and more memory to solve such systems in a reasonable time. For inverse problems constrained by time dependent PDEs, the adjoint method that is often employed to efficiently compute gradients and higher order derivatives requires solving a time-reversed, so-called adjoint PDE that depends on the forward PDE solution at each timestep. This necessitates the storage of a high dimensional forward solution vector at every timestep. Such a procedure quickly exhausts the available memory resources. Several approaches that trade additional computation for reduced memory footprint have been proposed to mitigate the memory bottleneck, including checkpointing and compression strategies. In this work, we propose a close-to-ideal scalable compression approach using autoencoders to eliminate the need for checkpointing and substantial memory storage, thereby reducing both the time-to-solution and memory requirements. We compare our approach with checkpointing and an off-the-shelf compression approach on an earth-scale ill-posed seismic inverse problem. The results verify the expected close-to-ideal speedup for both the gradient and Hessian-vector product using the proposed autoencoder compression approach. To highlight the usefulness of the proposed approach, we combine the autoencoder compression with the data-informed active subspace (DIAS) prior to show how the DIAS method can be affordably extended to large scale problems without the need of checkpointing and large memory.

Keywords Machine Learning · Autoencoder · Inverse Problems · High Performance Computing

1 Introduction

Modern supercomputers are an essential tool for today’s scientists and engineers, enabling them to simulate larger and more complex systems than ever before. The availability of large scale computing resources has enabled numerous breakthroughs in scientific knowledge in areas such as quantum computing [Liu et al., 2021c, Doi et al., 2019, Mandrà et al., 2021], computational chemistry [De Jong et al., 2010, Kowalski et al., 2021], drug discovery [Ge et al., 2013, Schmidt and Hildebrandt, 2017, Bharadwaj et al., 2021, Sukumar et al., 2021], biology [McFarlane and Biktasheva, 2008, Bukowski et al., 2010], and plasma physics [Bhattacharjee and Wells, 2021, Fedeli et al., 2022]. While the increased number of floating-point operations per second (FLOPS) has enabled larger and more challenging problems to be solved in reasonable amounts of time, applications are increasingly becoming bottlenecked by limited memory of computing systems — especially those applications dealing with *big data* [Denis et al., 2022, Imani et al., 2019].

There are at least three common approaches to mitigating this memory bottleneck: develop new algorithms that require less storage (for example, using density functional theory to approximate electron interactions rather than directly solving a many body problem in quantum mechanics [Bickelhaupt and Baerends, 2000]), utilize additional storage devices such as hard drives to increase the amount of data that can be stored, and trade extra computation for reduced storage requirements. Algorithmic improvement is always desirable, but is not always possible. Additionally, solving a closely related problem that has computational or storage advantages may cause a loss in accuracy. Serializing data to disk was previously only a viable solution for problems with high compute intensity. The high cost of reading from and writing to disk can be hidden when sufficient computation is performed. However, recent advances in storage technology such as non-volatile memory (NVM) have made serialization approaches more viable [Peng et al., 2020]. Indeed, NVM powers the large-memory nodes on Frontera, the Texas Advanced Computing Center’s largest supercomputer at the time of writing. This allows for traditional DRAM to be used as an extra level of cache [Wu et al., 2017, Stanzione et al., 2020]. The last mentioned approach, trading computation for storage, includes checkpointing methods [Wang et al., 2009, Zhang and Constantinescu, 2023, Griewank and Walther, 1997] and sparse decomposition [Zhao et al., 2020]. More generally, this means storing the inputs required to regenerate the desired output rather than storing the output directly [Akturk and Karpuzcu, 2018]. In addition to saving time, it is shown in [Akturk and Karpuzcu, 2018] that recomputation can have energy saving benefits over storing and retrieving data.

One type of problem that calls for advanced big data management techniques is full-waveform seismic inversion (FWI). As motivation, we give a high-level description of why advanced data management techniques are required for FWI here and give a detailed description in Section 2. FWI is a partial differential equation (PDE) constrained inverse problem with dependencies on both space and time derivatives. The dependency on time leads to the generation of large amounts of data. With spatio-temporal measurements of the velocity field, the inverse problem is to infer the underlying spatially varying material properties, namely the acoustic wave speed. Typical inverse solution methods reframe the problem as a constrained optimization problem and use gradient-based methods to minimize an objective function. Employing the adjoint approach [Giles and Pierce, 2000, Fichtner et al., 2006] to compute the gradient necessitates solving an adjoint PDE that is solved backward in time and depends on the corresponding forward solution at each timestep. As a result, *the entire solution history of the forward problem is needed in reverse order to solve the adjoint equation*. For large scale problems with high spatial resolution and many timesteps, storing the entire forward solution history is infeasible, requiring a different approach. As a quick back-of-the-envelope calculation, consider a domain with 1 billion degrees of freedom and 2 000 timesteps. Using a 4th order Runge-Kutta scheme to integrate in time, there are 4 solutions to be stored per timestep. Each solution has 6 fields — 3 velocity fields and 3 strain fields (assuming a velocity-strain formulation). This would require 384 TB to store in double precision. Perhaps one of the most commonly used techniques for such a problem is to employ checkpointing. Checkpointing is a technique whereby solutions are stored at only a select few timesteps and the rest discarded. The solution at any timestep can then be recreated by solving the forward problem from the nearest previous checkpoint. While reducing memory requirements, checkpointing effectively increases the computation requirements by 1 PDE solve per gradient evaluation.

An alternative approach employs compression to reduce both the memory requirements compared to full storage and computation requirements compared to the checkpointing case. The idea to use compression to mitigate the effects of limited memory or storage is not new. Compression techniques have been used extensively in the audio and video processing community for decades [Blessner, 1969, Lewis and Knowles, 1990]. There are two kinds of compression: lossless compression and lossy compression. Lossless compression is a class of techniques that are able to exactly recover the original input data. The PNG image format is an example of a format that employs lossless compression [Kaur and Choudhary, 2016]. The checkpointing strategy can be viewed as a form of lossless compression where information is encoded in the checkpoints and the physics model provides a decompression algorithm. Lossy compression, on the other hand, allows for errors to be made in reconstructing the input data. The JPEG protocol is an example of lossy compression in the image processing domain [Usevitch, 2001].

Various compression techniques have also been proposed to aid in scientific computation. Specific to the seismic inversion community, there are two main avenues of compression: compressing the source/receiver data [Habashy et al., 2011] and compressing the forward solution to avoid checkpointing. Source/receiver compression is useful in the case where large amounts of data are available, such as when many shots are recorded. The gradient must be evaluated at each shot; each requires the solution of the forward and adjoint PDEs, implying that the cost scales linearly in the number of shots [Duarte et al., 2020]. The goal of source/receiver compression is to find linear combinations of simultaneous sources and receivers that are (nearly) equivalent to the original problem. When the number of linear combinations required to closely replicate the original problem is small, the number of forward and adjoint solves required to compute a single gradient is much smaller, reducing both the memory footprint and the computation time [Habashy et al., 2011].

Several other works have already explored the idea of using compression to mitigate high adjoint-induced memory requirements [Cyr et al., 2015, Kukreja et al., 2019, Kukreja et al., 2022, Boehm et al., 2016]. Those works demonstrate that data can be compressed without negatively affecting the inverse solution and that compression can be faster than forward simulation. Several techniques of compressing in space as well as a spline interpolation technique for compression in time were proposed in [Boehm et al., 2016]. Results for a variety of off-the-shelf compression algorithms, including extensive results using the ZFP compression algorithm [Lindstrom, 2014], were given in [Kukreja et al., 2019]. Each of these papers demonstrates how different compression techniques can be used to solve seismic inverse problems on simple domains with large amounts of data. That is, the inverse problem is not ill-posed and regularization techniques are not required. While perturbations to the gradient due to compression may minimally affect the inverse solution in the case of large data, it is unclear that such approaches will be viable in solving ill-posed problems with limited data. Additionally, these approaches have limited compression capabilities, limiting the maximum problem size that can be solved.

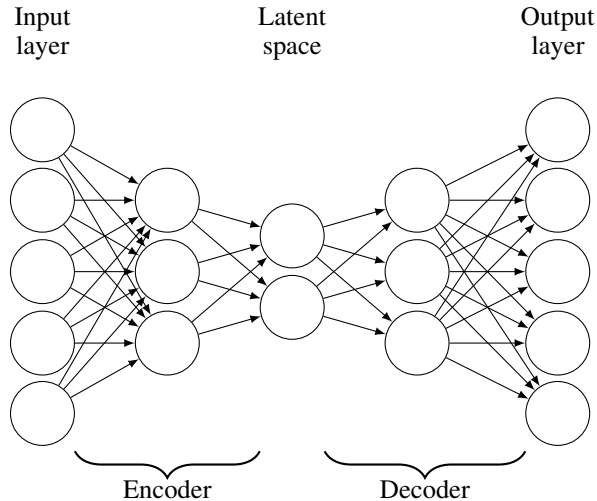


Figure 1: Autoencoder architecture with deep neural networks

Meanwhile, the scientific and technology communities have seen an explosion in the applications of machine learning techniques. Deep learning in particular has found fruitful application in enabling progress in speech recognition [Kamath et al., 2019], computer vision [Bjerge et al., 2022, Esteva et al., 2021], and in accelerating innovation in scientific computation [Reichstein et al., 2019, Kates-Harbeck et al., 2019]. One approach that has emerged is to use an autoencoder architecture to perform data compression [Cheng et al., 2018, Liu et al., 2021b, Hinton and Salakhutdinov, 2006]. An autoencoder is simply a deep neural network that approximates the identity map. The output at some intermediate layer can be extracted as a representation of the input and is referred to as the *latent representation* which resides in the *latent space* [Dillon et al., 2021]. Autoencoders are typically decomposed into two separate networks: an encoder which consists of the layers from the input to the latent space and a decoder which is a network that maps the latent space back to the original dimension. To achieve a compressed representation, the latent space must have dimension strictly smaller than the input. Compared to traditional dimension reduction methods, autoencoders can be viewed as a non-linear version of principal component analysis (PCA) [Ladjal et al., 2019, Kneer et al., 2021]. In the most simple case of a single layer encoder and single layer decoder with

linear activation, the autoencoder learns the same compression as PCA. That is, the single layer linear autoencoder projects the input data onto the same lower dimensional subspace that PCA identifies, though the representation is different [Baldi and Hornik, 1989, Ladjal et al., 2019]. The actual PCA basis vectors can be obtained from the weights of the trained encoder, showing the two are equivalent [Plaut, 2018]. The advantage of a deep autoencoder with nonlinear activations is that it is often able to achieve lower reconstruction error for the same dimension latent space compared to PCA [Liu et al., 2021a, Liu et al., 2021b], enabling higher feasible compression ratios in application.

While autoencoders have empirically demonstrated impressive compression ratios and low error rates, there is no theory that we are aware of at this time bounding the error of an autoencoder. However, a practical method of bounding the error of an autoencoder is to compute and store some form of the residual between the desired output (\mathbf{y}_{true}) and the actual output (\mathbf{y}_{pred}), i.e. $\mathbf{r} = \mathbf{y}_{\text{true}} - \mathbf{y}_{\text{pred}}$. Various techniques of approximately representing this residual vector have been proposed such as compressing \mathbf{r} with an off-the-shelf algorithm when $\|\mathbf{r}\| > \text{tol}$ for some tolerance, tol [Lee et al., 2022, Liu et al., 2021a] or storing only the elements r_i of \mathbf{r} where $|r_i| > \text{tol}$ [Liu et al., 2021b, Abu Alsheikh et al., 2014].

To address the problems of additional expensive PDE solves required by the checkpointing approach and the limited compression capability of off-the-shelf compression techniques, we propose a novel autoencoder approach for compressing the forward solution. We show empirically that this compression method is faster than the checkpointing method while achieving comparable solution accuracy. In addition to showing that a trained autoencoder has memory and computational advantages over existing methods, we develop an efficient data generation and training procedure based on the Bayesian inversion formulation that enables our approach to maintain its advantages, even when including the cost of training the autoencoder. While variations of autoencoders are often used for generative modeling [Kingma and Welling, 2013] and others assign a physical interpretation to the latent space [Goh et al., 2019], we use the *auto-encoding* capabilities of the autoencoder architecture to allow the training process to find the most effective compressed latent representation for seismic input data. We provide a mathematical description of the FWI problem and the inverse problem in Section 2. Two autoencoder compression variants are proposed in Section 3 along with detailed explanation of autoencoder architecture, training data selection, and normalization. We show in Section 4 that machine learning can be leveraged to accelerate the solution of seismic inverse problems in very high dimensions, even in the ill-posed case with few measurements. Through numerical experiment, we show that this approach is faster than the checkpointing approach, and as fast as the state-of-the-art off the shelf compression approach, ZFP [Lindstrom, 2014], while achieving much higher compression ratios. We then extend the data informed active subspace (DIAS) regularization method [Nguyen et al., 2022] to nonlinear problems and show that autoencoder compression can be used to enable the affordable application of the DIAS prior for large-scale inverse problems.

2 Full Waveform Inversion

As a simplified model of the earth’s seismic properties, we consider the acoustic wave equation. In velocity-strain form, this gives rise to a system of first order PDEs. We choose the velocity-strain form because of its close relation to the acoustic-elastic wave equation [Wilcox et al., 2015]. This enables simultaneous derivation of gradients and Hessians for both acoustic, elastic, and acoustic-elastic formulations. Additional computational and mathematical advantages can be found in [Wilcox et al., 2015]. Following the setup given in [Bui-Thanh et al., 2013], the acoustic wave equation is given by,

$$\rho \frac{\partial \mathbf{v}}{\partial t} - \nabla (\rho c^2 e) = \mathbf{g}, \quad (1a)$$

$$\frac{\partial e}{\partial t} - \nabla \cdot \mathbf{v} = 0, \quad (1b)$$

where $\rho = \rho(\mathbf{x})$ is the density, $c = c(\mathbf{x})$ is the acoustic wave speed for which we are inverting, $\mathbf{g} = \mathbf{g}(\mathbf{x}, t)$ is a forcing function, $\mathbf{v} = \mathbf{v}(\mathbf{x}, t)$ is the velocity vector, $e = e(\mathbf{x}, t)$ is the trace of the strain tensor (dilatation), and \mathbf{x} denotes the spatial coordinate in the domain Ω . We specify initial conditions for the velocity and dilatation fields

$$\mathbf{v}(\mathbf{x}, 0) = \mathbf{v}_0(\mathbf{x}) \quad \text{and} \quad e(\mathbf{x}, 0) = e_0(\mathbf{x}), \quad \mathbf{x} \in \Omega. \quad (2)$$

Lastly, we impose traction-free boundary conditions

$$e(\mathbf{x}, t) = 0, \quad \mathbf{x} \in \Gamma = \partial\Omega, \quad t \in (0, T)$$

with final time T . The 3 components of the velocity vector field and the 3 diagonal components of the strain tensor field, used to compute the dilatation, will be collectively referred to as the *state* variables in the rest of this paper. It is the state variables that need to be compressed and decompressed.

In this work, we consider the inverse parameter estimation problem — inferring the wave speed $c(\mathbf{x})$ from sparse measurements of the velocity, \mathbf{d} . Since we consider the setting with limited measurements, the inverse problem is

ill-posed and regularization is required. The inverse problem can be formulated as the optimization problem

$$\mathbf{u}^* := \arg \min_{\mathbf{u}} \frac{1}{2} \|\mathcal{F}(\mathbf{u}) - \mathbf{d}\|_{\Gamma_{\text{noise}}^{-1}}^2 + \frac{1}{2} \|\mathbf{u} - \mathbf{u}_0\|_{\Gamma_{\text{prior}}^{-1}}^2 \quad (3)$$

where \mathbf{u} is referred to as the parameter of interest (PoI), \mathcal{F} is the parameter to observable map (PtO map), Γ_{noise} is the noise covariance matrix of the observations \mathbf{d} , \mathbf{u}_0 is the initial guess and Γ_{prior} characterizes the regularization. In the Bayesian setting [Kaipio and Somersalo, 2006], \mathbf{u}_0 and Γ_{prior} are interpreted as the prior mean and prior covariance matrix, respectively. While we consider full waveform inversion in the deterministic setting, it is convenient to consider the problem in the Bayesian framework and only work toward estimating the maximum a posteriori (MAP) point. The statistical framing of the MAP problem allows us to choose regularization via selection of a prior distribution rather than ad-hoc and allows for trivial extension of our proposed compression approach to quantifying uncertainty. In our case, the PoI is the acoustic wave speed which is mapped to our observations, \mathbf{d} , by solving the acoustic wave equation and observing the velocity field only at the receivers. Let $\mathbf{u} \approx c$ be the discretized acoustic wave speed that we will numerically estimate. Then

$$\mathcal{F} := B\mathcal{A}$$

where \mathcal{A} is the solution of (1) and B is an observation operator, extracting the velocity field at receiver locations.

As in [Bui-Thanh et al., 2013], we choose the prior to be the PDE-based BiLaplacian which encodes smoothness and anisotropy of the wave speed along with our certainty about our initial guess. The BiLaplacian prior term $\frac{1}{2} \|\mathbf{u} - \mathbf{u}_0\|_{\Gamma_{\text{prior}}^{-1}}^2$ is computed by solving the following elliptic PDE:

$$-\alpha \nabla \cdot (\Theta \nabla \mathbf{u}) + \alpha \mathbf{u} = s \quad \text{in } \Omega \quad (4a)$$

$$\alpha (\Theta \nabla \mathbf{u}) \cdot \mathbf{n} = 0 \quad \text{on } \partial\Omega \quad (4b)$$

where \mathbf{n} is the outward facing unit normal on the boundary, $\partial\Omega$. $\Gamma_{\text{noise}}^{-1}$ is the square of this differential operator. Properties of this prior and further discussion can be found in [Bui-Thanh et al., 2013]. Finally, derivation of the discrete forward, adjoint, and gradient expressions for a discontinuous Galerkin discretization can be found in [Wilcox et al., 2015].

3 Compression methods

There are a variety of ways that the state variables can be compressed. Each state variable is a function of time and 3 space dimensions, resulting in 4 dimensions across which the state can be compressed. Additionally, there might be some relationship between the state variables that could be exploited to achieve higher compression ratios. In this work, we propose two compression techniques that are amenable for implementation with autoencoders, treating each state variable independently:

1. Compression in space, allowing the autoencoder to discover the 3D structure of the state across multiple elements.
2. Compression in time on an element-by-element basis.

As a brief justification for pursuing only these two compression setups, let us make a few notes. First, there is potential for scale mismatch between each of the state variables. Consider again equation (1b). The time derivative of the dilatation is related to the divergence of the velocity field. From this we can see that there could be very large velocities, but no dilatation if the velocity field is divergence free. This makes it difficult to design a method that can garner any correlation between the *value* of the velocity field at a given timestep and the *value* of the strains.

Secondly, we decided against pursuing methods requiring explicit specification of the fields in three-dimensional coordinates. That is, we treat all the nodal coefficients equally, not explicitly taking advantage of the embedding of these nodal coefficients in 3-dimensional space. While it is in principle possible to use something like a convolutional neural network with 3-dimensional kernels [Ji et al., 2012], we found two major difficulties: 1) convolutional neural networks in 3D are rather slow and 2) the nodes of our DG mesh are not equally spaced. Although equally spaced nodes would enable simple application of convolutional autoencoders, non-uniformly spaced nodal coordinates such as Gauss-Lobatto-Legendre (GLL) enable more accurate integration [Quarteroni et al., 2010] and are a natural choice for node location in a DG scheme. In Sections 3.1 and 3.2, we will present the implementations of the two proposed autoencoder compression approaches.

3.1 Compression on a uniform mesh

Consider a box domain where $\Omega = [0, 1]^3$. Such a domain may arise in reservoir exploration, the example used in [Kukreja et al., 2019]. Figure 2 shows the mesh on a box domain. While the nodes are unevenly spaced, they occur in a regular pattern. This allows us to flatten a state variable across multiple elements into a single vector for compression. Care must be taken to partition the domain evenly across MPI ranks and to ensure that each rank stores the nodes in the same spatial orientation, i.e. the elements are stacked the same way in memory on each rank. The autoencoder then has the freedom to identify the most relevant spatial correlation in order to most accurately compress the data. Note that the order in which the elements are stacked does not matter so long as it is the same across all ranks since a permutation can be implicitly learned. With the same state layout on every rank, a single autoencoder can be trained that compresses the local degrees of freedom on a single rank. Once trained, each rank stores its own copy of the autoencoder, eliminating the need for any communication. The fact that no communication is required is key to the scalability of our proposed approach.

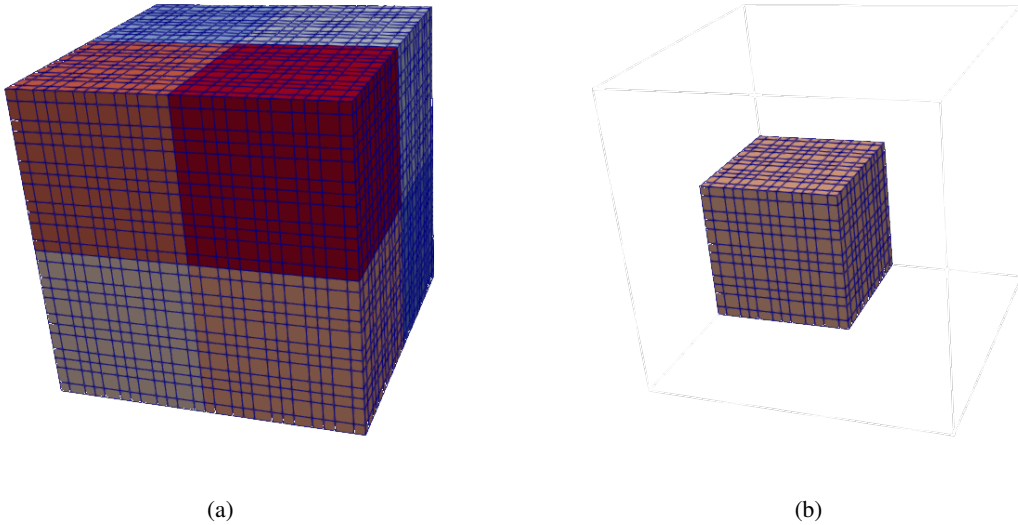


Figure 2: (a) Course mesh on box domain showing non-uniform spacing of grid. Different colors correspond to different MPI ranks. (b) mesh of single MPI rank consisting of 8 third order elements.

There are a few competing factors that must be balanced in designing an autoencoder for compression. The input vector should be:

1. Large enough so that a high compression ratio can be attained with low reconstruction error.
2. Small enough so that the autoencoder runs quickly.

The second item poses a particular challenge in the present case as the DG solver used to solve the forward acoustic wave equation is highly tuned. Special care must be taken in order to develop a method that is faster than checkpointing while maintaining sufficient accuracy. We found empirically that an input dimension of 4096 adequately balanced these two constraints. This corresponds to 8 elements per MPI rank with 3rd order polynomials, resulting in 64 nodes per element (4^3).

3.2 Compression on non-uniform mesh

While using an autoencoder to compress in space is intuitive and simple to implement, there are severe limitations to the practical applications of such an approach. First, each MPI rank must have the exact same number of degrees of freedom that are arranged in exactly the same manner in order to avoid padding or communicating ghost elements. This is because autoencoders that employ dense hidden layers have a fixed input size. Unless extreme care is taken, this requires that the mesh be uniformly refined and have no hanging nodes. Such a restriction poses major challenges for problems with a non-rectangular domain or when non-hexahedral elements are desired. To mitigate these limitations, we propose to compress along the time dimension, treating each element as an independent state. This method works seamlessly with h-adaptive mesh refinement (refining the mesh geometry), though p-adaptivity (changing the polynomial order of the element) remains a challenge. For this work, we only consider algorithms with h-adaptivity.

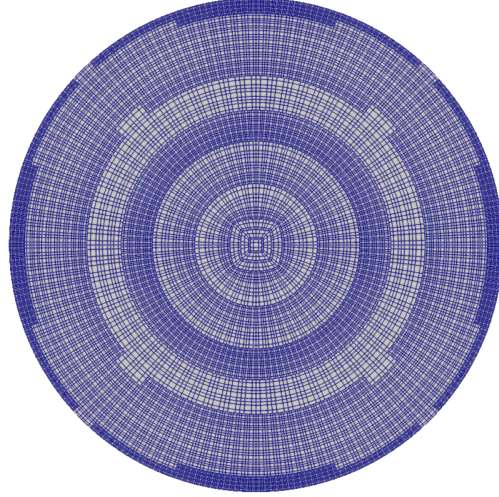


Figure 3: A cross-section of the earth domain with h-adaptive mesh refinement. Notice the non-uniform character of the mesh, with very small elements near the crust required to resolve the seismic waves.

To demonstrate the success of this approach, we consider solving a seismic inverse problem on a spherical domain. We employ h-adaptive mesh refinement to ensure that the seismic waves can be resolved on each element with at least 3 nodes per wavelength. Figure 3 shows a cross section of the mesh. Hanging nodes that result from local mesh refinement pose no problem for our proposed compression strategy since each node is considered independently.

The same constraints as discussed in Section 3.1 apply in this scenario. Similar to the box domain case, we found that an input dimension to the autoencoder of 4096 worked well. Since we use a 4th order Runge-Kutta (RK) explicit timestepping scheme [Quarteroni et al., 2010], a 4096 dimensional input vector results from using 3rd order polynomials (64 nodes per element) and 16 timesteps, each with 4 RK stages.

3.3 Autoencoder architecture and training details

Any discussion of results obtained using deep learning would be incomplete without a discussion of the architecture used to obtain the results. While the order of the data differs between space compression and time compression methods, the same autoencoder architecture can be used in either case since the input and output dimensions are the same. The difference between the trained autoencoders used for each compression method lies solely in the training data. Table 1 shows the architecture design of both the encoder and the decoder. All layers are “dense” layers, which corresponds to an affine transformation followed by a nonlinear activation. We found the exponential linear unit (ELU) to perform better than the rectified linear unit (ReLU), hyperbolic tangent (tanh), and sigmoid activations. The ELU activation function is given by

$$\text{ELU}(y) := \begin{cases} e^y - 1 & \text{if } y < 0 \\ y & \text{else.} \end{cases}$$

Table 2 shows the relevant hyperparameters of the training process. Training took approximately 3 hours using two Nvidia 2080Ti GPUs.

As mentioned in Section 3.1, it is difficult to design an autoencoder compression system that both performs well in terms of accuracy and compression ratio while also being fast. Recall that the evaluation of a single dense layer requires the computation of

$$\sigma(\mathbf{y}\mathbf{W} + \mathbf{b}). \quad (5)$$

Considering the first layer of the encoder, $\mathbf{W}_1 \in \mathbb{R}^{4096 \times 512}$, $\mathbf{y} \in \mathbb{R}^{4096}$ and $\mathbf{b}_1 \in \mathbb{R}^{512}$. There are 2,097,152 entries in the matrix \mathbf{W}_1 . Compare this to the second layer which has a weight matrix $\mathbf{W}_2 \in \mathbb{R}^{512 \times 256}$ and 131,072 entries. The first layer then has 16 times more entries in the weight matrix than the second layer. Further layers of the encoder have even smaller weight matrices. It is clear that the dominant cost in compressing a vector is the computation of the first matrix-vector multiply, $\mathbf{y}\mathbf{W}_1$. To mitigate this cost, we develop a hybrid sparse-dense architecture whereby the first layer of the encoder and last layer of the decoder are trained to be 95% sparse.

	Encoder	Decoder
Input dimension	4096	64
Output dimension	64	4096
# hidden layers	7	7
Neurons per hidden layer	[512, 256, 256, 256, 128, 64, 64]	[128, 128, 256, 256, 256, 512, 4096]
Activation	ELU	ELU

Table 1: Autoencoder architecture and hyperparameters used to train network.

Precision	float32
Optimizer	LAMB [You et al., 2019]
Initial learning rate	10^{-3}
Learning rate decay	$lr = 0.5lr$ applied every 5 epochs
Epochs	20
Batch Size	512
# GPUs	$2 \times 2080Ti$

Table 2: Training hyperparameters used to fit autoencoder weights and biases to data.

As an example to show the improvement of the sparse-dense architecture over the fully dense architecture, consider compressing a *batch* of 864 vectors each with size 4096. Since evaluating the output of the neural network requires nothing more than matrix-vector multiplications, vector additions, and element-wise application of an activation function, all 864 vectors can be processed simultaneously by stacking into rows. Then the input \mathbf{y} has shape (864, 4096). Timing results for both the encoder and decoder on a single core of an Intel Xeon Platinum 8280 CPU on Frontera are shown in Table 3. We would then expect approximately a 50% speedup with the sparse-dense architecture over the fully dense architecture.

	Encoder	Decoder
Fully dense	102 ms	140 ms
Hybrid sparse-dense	40 ms	79 ms

Table 3: Comparison of timings of fully dense architectures vs hybrid sparse-dense architecture for encoder and decoder for compressing/decompressing 864 vectors on a single core of an Intel Xeon Platinum 8280 CPU.

Unfortunately, the application setting is slightly different since all cores are used rather than just a single core. Consider the same test case replicated on each CPU core simultaneously. There are 56 cores across 2 sockets on a single node of Frontera. Since each task executes independently with no communication, we might expect perfect scaling and for the test to complete in the same amount of time. However, there are now more cores contending for data with limited cache and memory bandwidth. Indeed, in the first case, 864 single precision input vectors require only 14.2 MB to store. This easily fits in the 38.5 MB of L3 cache of a single Intel Xeon Platinum 8280 [int,]. Furthermore, the weights of the fully dense encoder require only 17.8 MB to store. The input data and the entire encoder can fit in L3 cache! Since L3 cache is shared among all cores of this CPU, bytes must be streamed from main memory when all cores are running simultaneously. Table 4 shows the timings for the encoder and decoder with the fully dense and hybrid sparse-dense architectures when running on all cores.

Although there is still significant advantage in using the hybrid architecture for the decoder, the evaluation of the encoder proves to be faster using the fully dense architecture than the hybrid architecture when all 56 cores are being utilized. We are unsure why this is the case at the time of writing and further optimization is a topic for future investigation. However, measuring the performance showed that we could achieve faster compression by using a fully

	Encoder	Decoder
Fully dense	110 ms	160 ms
Hybrid sparse-dense	120 ms	117 ms

Table 4: Comparison of timings of fully dense architectures vs hybrid sparse-dense architecture for encoder and decoder for compressing/decompressing 864 vectors on 56 cores of 2 Intel Xeon Platinum 8280 CPUs on a single node of the Frontera supercomputer.

dense matrix for the weights of the first layer while optimizing the evaluation time of the decoder using a sparse matrix for the final layer. Because of the strict speed requirements, we do not utilize any error bounding methods which require the computation and potential storage of a residual vector [Lee et al., 2022, Liu et al., 2021a, Liu et al., 2021b, Abu Alsheikh et al., 2014].

3.3.1 Training data

One common criticism of deep learning methods is that large training datasets are often required for the DNN to perform well in practice. In the case of compression, other algorithms such as those implemented in the ZFP package [Lindstrom, 2014] do not require training data. Even when deep learning methods may perform well on training data, they may perform poorly in practice when the training dataset is not sufficiently large, a concept referred to as *generalization error*. While this is true, we argue that the cost of training an autoencoder is a one-time upfront cost. Further, data generation and training require several orders of magnitude fewer compute node-hours than solving the inverse problem. In this section, we detail the data generation process.

Consider a statistical interpretation where the training data $\mathbf{y} \in \mathbb{R}^n$, is drawn from some distribution, $\pi(\mathbf{y})$. Suppose that we have a dataset of N samples $\mathcal{D}^N = \{\mathbf{y}^1, \dots, \mathbf{y}^N\}$ where $\mathbf{y}^i \sim \pi(\mathbf{y})$. Let $\Psi_{\mathcal{D}^N}(\mathbf{y})$ denote the output of the machine learning algorithm after being trained with dataset \mathcal{D}^N . A common metric for evaluating the performance of any machine learning algorithm is the *generalization error*. Given some loss function denoted $\mathcal{L}(\Psi(\mathbf{y}), \mathbf{y})$, such as mean squared error,

$$\mathcal{L}_{\text{MSE}}(\Psi(\mathbf{y}_{\text{true}}), \mathbf{y}_{\text{true}}) := \frac{1}{n} \|\mathbf{y}_{\text{true}} - \Psi(\mathbf{y}_{\text{true}})\|_2^2,$$

the generalization error for an autoencoder is $\mathbb{E}_{\pi(\mathbf{y})}[\mathcal{L}(\Psi(\mathbf{y}), \mathbf{y})]$ [Nadeau and Bengio, 1999]. That is, the generalization error is the average loss over the entire distribution $\pi(\mathbf{y})$.

Generalization error plays an important role in designing a data generation process. There are two ways one can reduce the generalization error:

1. Increase the size of the training dataset by drawing more samples from $\pi(\mathbf{y})$.
2. Choose $\pi(\mathbf{y})$ so that it can be well-approximated with few samples.

The second method can be interpreted as choosing the most narrow distribution that is appropriate for the application at hand. We will explore how this option can be used in the context of generating data for seismic inversion. For typical machine learning applications, this may not be possible as we don't know $\pi(\mathbf{y})$. The Bayesian inversion setting makes this possible for our application, as we discuss next.

In order to compress seismic data, we need to generate examples similar to the states that will be seen in application. One way to do this is to solve the acoustic wave equation and save some of the data for training. However, it is still unclear which solutions of the wave equation should be included in the training dataset. Should we try to train the autoencoder to compress and decompress all possible solutions to the wave equation on a given domain? There are clearly wave equation solutions that are not relevant for our application. Mathematically, the challenge becomes defining the relevant distribution $\pi(\mathbf{y})$. The Bayesian framework [Kaipio and Somersalo, 2006] helps us to choose a good distribution for generating data. Bayes' formula tells us,

$$\pi_{\text{post}}(\mathbf{u}|\mathbf{d}) \propto \pi_{\text{like}}(\mathbf{d}|\mathbf{u}) \pi_{\text{prior}}(\mathbf{u}). \quad (6)$$

This can be interpreted as the likelihood, $\pi_{\text{like}}(\mathbf{d}|\mathbf{u})$, updating the prior density, $\pi_{\text{prior}}(\mathbf{u})$, based on observed data, \mathbf{d} , to produce the posterior density, $\pi_{\text{post}}(\mathbf{u}|\mathbf{d})$, [Scales and Tenorio, 2001]. The observations \mathbf{d} are related to the states that will be compressed, denoted \mathbf{y} here, through an observation operator, i.e. $\mathbf{d} = \mathbf{B}\mathbf{y}$. Since the posterior density is the product of the likelihood and the prior, the posterior density is non-zero only where the prior density is non-zero. That is, the posterior lies within the support of the prior. Therefore, we are only interested in whether the autoencoder

performs well in compressing states, \mathbf{y} , that can be generated by samples from the prior. We can generate relevant examples of possible states by solving the acoustic wave equation with the PoI (the wave speed) set to samples from the prior. The autoencoder does not need to perform well on every possible state that could be generated from the wave equation, it only needs to work well on states generated by solving the wave equation with parameters sampled from the prior.

With motivation from statistical learning theory and Bayesian inverse problems, we now detail an algorithm for generating training data. The compression data structure is a vector that stores the state variables in the order

Algorithm 1 Data generation algorithm for training compression autoencoder

Input: number of samples, n ; final time, T

```

1: for  $i = 1, \dots, n$  do
2:    $c =$  random draw from prior
3:   for  $t = 1, \dots, T$  do
4:     Solve acoustic wave equation for one timestep
5:     Consolidate states,  $\mathbf{v}$ ,  $e$ , into compression data structure
6:     if Data structure is full then
7:       Write data structure to file
8:     end if
9:   end for
10: end for

```

corresponding to the compression scheme in use. This setup allows any ordering to be used and for training data to automatically have the correct ordering — reducing effort to set up the training pipeline. Algorithm 1 can generate large amounts of data very quickly. For the earth-scale problem with an 11.2 million DoF mesh, several terabytes can be generated in only a few minutes. To reduce the amount of data written to file, we randomly chose whether to write or discard the data structure. On 32 nodes of Frontera, solving the wave equation and writing to file takes on the order of 1 minute. With 10 draws from the prior, keeping only 0.1% of the data, we generated 50 GB of training data in less than 1 hour. The total cost of data generation is then $\mathcal{O}(10)$ node-hours.

Finally, we discuss normalization of the training data. The states have scales that vary between 10^{-16} and 10^5 over the solution of (1). It would be difficult for an autoencoder to be able to accurately compress and decompress states with such widely varying scales, especially in single precision. To reduce the burden on the autoencoder of learning scale, we normalize the data between 0 and 1. This enables us to store the scale and offset of the data in double precision while capturing the relative variation of the data in single precision. Consider an arbitrary state vector that will be compressed, denoted \mathbf{y} following the notation in (5). Let \mathbf{y}_{true} be a consolidated state vector that will be compressed (state DoFs consolidated either in space or in time). The input vector to the encoder, \mathbf{y} , is then given by

$$r = \max(\max(\mathbf{y}_{\text{true}}) - \min(\mathbf{y}_{\text{true}}), \beta)$$

$$\mathbf{y} = (\mathbf{y}_{\text{true}} - \min(\mathbf{y}_{\text{true}})) / r.$$

In order to avoid division by zero, r is set to be at least some tolerance, β . We choose $\beta = 10^{-7}$.

4 Numerical results

In this section we present numerical results showing the efficacy of our proposed autoencoder compression approach for both spatial compression on the box domain problem (Section 3.1) and temporal compression on a spherical domain (Section 3.2). For both problems, we solve the inverse problem using a Newton conjugate gradient (NewtonCG) method [Yang, 2009, Epanomeritakis et al., 2008]. In each conjugate gradient iteration, the action of the Hessian on a vector is required which entails solving two additional linearized PDEs, referred to as the incremental forward problem and incremental adjoint problem. Expressions for these PDEs in the case of the acoustic wave equation can be found in [Bui-Thanh et al., 2012]. The incremental forward problem relies on the solution of the forward problem at each timestep and so requires decompression as well. The incremental adjoint problem requires the solution of both the forward and incremental forward problems, and thus requires another decompression of the forward states. Empirically, we find that the gains of decompression are mostly offset by the costs of compression. However, the states only need to be compressed once per Newton iteration and are potentially decompressed many times. That is, the cost of compression is amortized over every evaluation of the adjoint, incremental forward, and incremental adjoint problems within a single Newton iteration. While it is also possible to compress and decompress the incremental forward problem, it is not explored in this paper since each incremental forward solution is only re-used once.

4.1 Results: compression in space

We demonstrate the compression in space approach on a cube domain with all sides of length 1km. Five sources are located at 1m depth and 1089 receivers are evenly spaced at the surface, observing the velocity field for 3 seconds. The sources are Ricker wavelets in time, smoothed by convolving with a narrow Gaussian in space. The source term for a source at \mathbf{x}_0 is then given by

$$\mathbf{g}(\mathbf{x}, t; \mathbf{x}_0) = \rho(\mathbf{x}) \frac{1}{\sqrt{2\pi}\sigma_x} e^{-\frac{\|\mathbf{x}-\mathbf{x}_0\|_2^2}{2\sigma_x^2}} \left(1 - \frac{(t-t_c)^2}{\sigma_t^2}\right) e^{-\frac{(t-t_c)^2}{2\sigma_t^2}} [0, 0, -1]^T.$$

In this case, we consider a wavelet centered at $t_c = 0.6$ seconds with $\sigma_t = \frac{1}{\pi}$ and $\sigma_x = 0.05$.

A snapshot of the velocity magnitude is shown in Figure 4a. Following the setup in Section 3.1, we show both speedup and absolute error results compared to the checkpointing solution. While the synthetic true solution is our target, our compression strategy aims to replace checkpointing as a means for managing limited memory, not to change the inverse solution. Therefore, the appropriate comparison is with the inverse solution computed using checkpoints rather than the true solution. Similar to the earth problem, we invert for a variation in the background wavespeed field. A box-shaped inclusion is introduced into the domain, shown in Figure 4b, and is referred to as the anomaly.

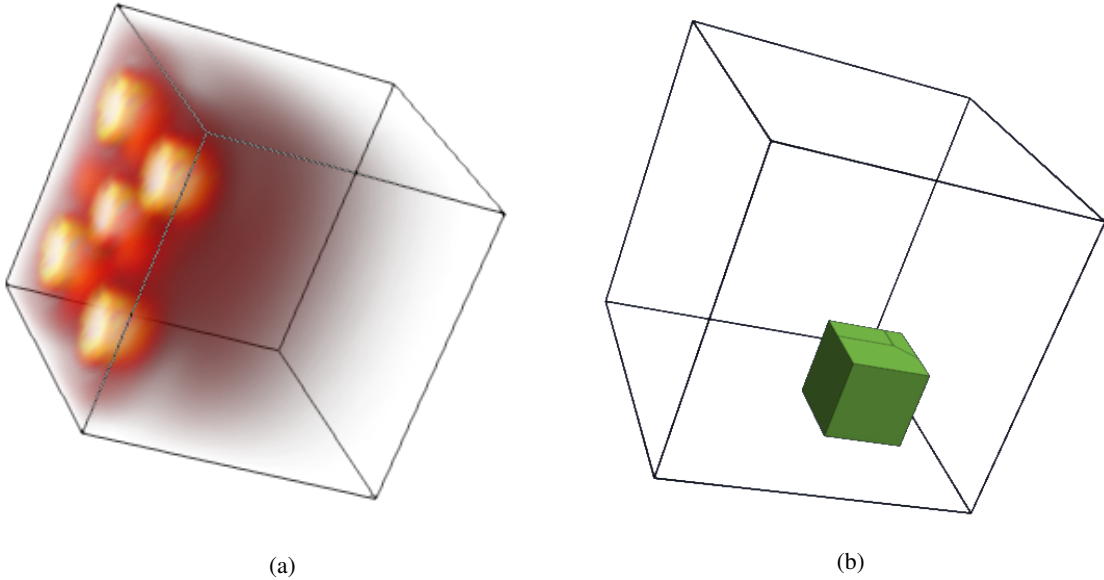


Figure 4: (a) Snapshot of velocity magnitude at 1.2 seconds (b) Inclusion in background wave speed.

To demonstrate the weak scaling of this method, we show results for several refinement levels, each refinement increasing the total number of degrees of freedom by 8 times. Table 5 shows the speedup compared to the checkpointing solution. While the overall speedup may not be very impressive, it is not the only objective of our proposed compression approach. As we have discussed, the other objectives are to reduce memory footprint and to eradicate checkpointing. Furthermore, there is a maximum speedup of $1.3\times$ for the gradient since the time to solve the forward problem, the adjoint problem, and evaluate the gradient are approximately equal. That is, the cost of computing the gradient in the ideal case is 3 PDE solves while the checkpointing case requires 4 PDE solves. Thus, the speedup of 1.22 for the largest mesh in Table 5 is close to ideal. Similarly, the Hessian-vector product computation has the maximum speedup of 1.5 (requiring 4 PDE solves in the ideal case vs 6 PDE solves with checkpointing), and the speedup of 1.27, without compressing the incremental forward solve, for our compression approach is already an achievement. Furthermore, the acoustic wave equation, (1), is linear and not difficult to solve with explicit time stepping. Our proposed approach would show closer to ideal speedup when used to replace implicit solvers or when used on nonlinear problems with much more time consuming forward solves since the cost of autoencoder compression only depends on the number of parameters of the neural network. Table 5 shows that the speedup approaches the ideal one and the relative error decreases as the number of DoFs increases. A cutaway of the inverse solution with the largest mesh for both the checkpointing case and the autoencoder compression case is shown in Figure 5. The fact that the anomaly reconstructions are visibly indistinguishable is due to 0.4% difference.

Mesh DoFs	Cores	∇ Speedup	$\mathcal{H}v$ Speedup	Relative l_2 Error %
4,096	1	1.06	1.20	1.7
32,768	8	1.19	1.26	0.7
262,144	64	1.17	1.22	0.6
2,097,152	512	1.17	1.23	0.7
16,777,216	4096	1.22	1.27	0.4

Table 5: Speedup of the autoencoder compression algorithm compared to the checkpointing solution. ∇ represents the gradient and $\mathcal{H}v$ represents a Hessian-vector product. The speedup approaches the ideal speedup as the number of DoFs increases while the relative error decreases.

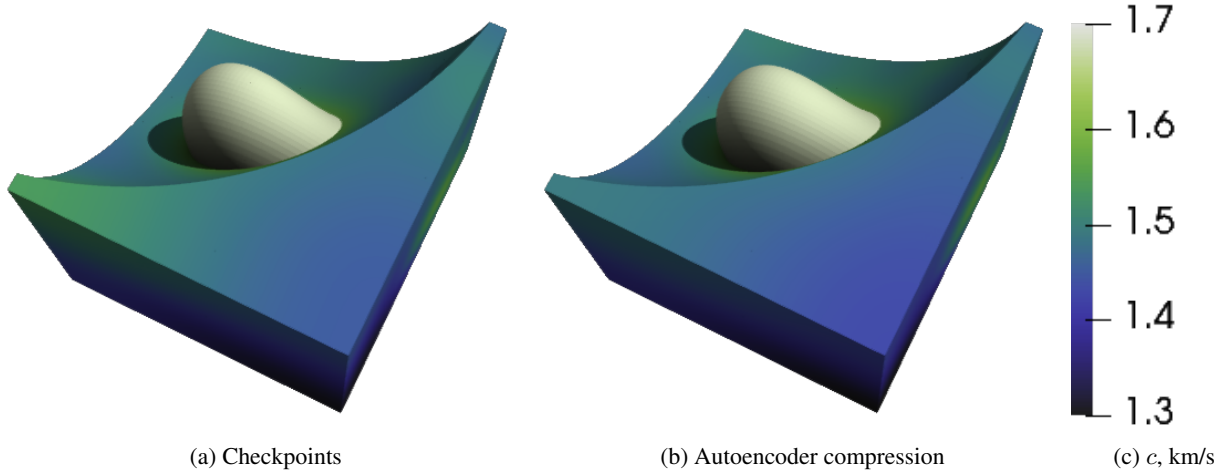


Figure 5: Inverse solutions on box domain using (a) checkpoints and (b) autoencoder compression in space for problem with 16,777,216 DoF mesh. The solutions have the same color scale with the inclusion rendered as an isosurface at 1.67 km/s.

4.2 Results: compression in time

While it is intuitive that seismic waves exhibit strong spatial redundancy and thus have high compressibility, it is not immediately obvious that temporal compression schemes will yield acceptable results. We test the temporal compression scheme presented in Section 3.2 on the earth-scale seismic inverse problem. We build upon the framework established in [Bui-Thanh et al., 2012, Bui-Thanh et al., 2013] to show that our proposed compression scheme is a viable method for large-scale seismic inverse problems. The results shown here follow the setup of Case II from [Bui-Thanh et al., 2013]. There are 3 source locations in the Northern Hemisphere, one at the North Pole and two placed at 90 degree increments along the equator. Here, we consider sources modeled as Dirac delta functions in space centered at the source location, \mathbf{x}_0 , and a Gaussian in time given by

$$\mathbf{g}(\mathbf{x}, t; \mathbf{x}_0) = \frac{1}{\sqrt{2\pi}\sigma} \delta(\mathbf{x} - \mathbf{x}_0) e^{-\frac{(t-t_c)^2}{2\sigma^2}}$$

where $t_c = 60$ seconds and $\sigma = 20$ seconds. We place 130 receivers spaced at 7.5 degree increments throughout North America as show in Figure 6, measuring the velocity field. Additive noise with standard deviation 0.002 is introduced into the data. The earth is modeled as a sphere with radius 6,371km. Both the sources and receivers are buried at 10km depth.

Course meshes cannot resolve the sufficiently high frequency waves required to effectively image the earth and thus may not be used. We found that a maximum frequency resolution of 0.05Hz was sufficient to obtain good inversion results. Thus, the smallest domain size that we consider has a mesh with 11.2 million degrees of freedom. This corresponds to a discontinuous Galerkin discretization with 174,481 elements using 3rd order polynomials. We solve this problem on 64 nodes (3,584 CPU cores) of Frontera running for 10 hours. Speedup results compared to the checkpointing case are shown in Table 6. Here we report the average relative l_2 error of the solution obtained using autoencoder

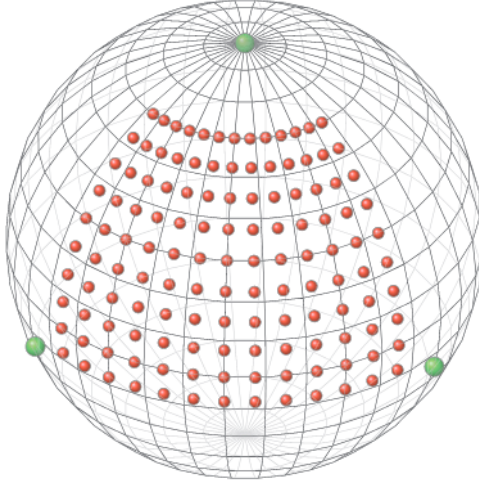


Figure 6: Three sources shown in green at the North Pole and along the equator. 130 receivers shown in red distributed in North America spaced 7.5 degrees apart. Figure from [Bui-Thanh et al., 2013], Copyright ©2013 Society for Industrial and Applied Mathematics. Reprinted with permission. All rights reserved.

compression to the solution obtained using checkpointing. Similar to the box domain, there is greater speedup in the $\mathcal{H}v$ product computation than the gradient computation due to paying the cost of compression during the gradient solve. The difference in speedup between the box problem and the earth problem is likely due to variable per-process problem size induced by the non-uniform spherical mesh and related cache contention issues. As mentioned in Section 3, cache effects can greatly impact the performance of the compression algorithm.

Mesh DoFs	∇ Speedup	$\mathcal{H}v$ Speedup	Relative l_2 error %
11,166,784	1.05	1.17	0.03

Table 6: Speedup of the autoencoder compression algorithm compared to the checkpointing solution. ∇ represents the gradient and $\mathcal{H}v$ represents a Hessian-vector product. Timing results were obtained by running on 64 nodes (3,584 CPU cores) of the Frontera supercomputer.

To demonstrate scalability of the autoencoder compression approach, we solve the same problem on a refined mesh with 139,227,136 DoFs. The full state vector (3 velocities and 3 strains) then has 835,362,816 DoFs. This problem was solved on 256 nodes of Frontera (14,336 CPU cores). Table 7 compares the autoencoder compression results to the checkpoint solution. We find that there is a slight reduction in terms of gradient speedup and a slight increase in speedup of the Hessian-vector product compared to the course mesh solution detailed in Table 8. One possible reason for the decrease in speedup of the gradient computation is the increased per-process work of the larger problem. The smaller problem with 11 million mesh DoFs has an average of 4,681 mesh DoFs per process, while the larger problem has an average of 9,711 mesh DoFs per process. We explored the effects of limited cache size on the timing of autoencoder compression in Section 3 and found that the compression is more sensitive to cache effects than decompression, at least for our implementation. It is therefore not surprising that the speedup of the gradient computation, which includes the cost of compression, is reduced when each process is responsible for compressing a larger amount of data. While speedup is desired in all computations, there is an order of magnitude more Hessian-vector products than gradient computations required to compute the MAP solution, with $\mathcal{O}(100)$ $\mathcal{H}v$ products and $\mathcal{O}(10)$ gradient evaluations. The overall cost is dominated by $\mathcal{H}v$ products, and so the observation that the gradient computation sees no speedup from compression has little impact on the total computation time.

Having shown that autoencoders are a viable compression technique for accelerating seismic inverse problems, we now compare our results to the state-of-the-art off-the-shelf compression technique proposed for seismic inversion in [Kukreja et al., 2019]. While other off-the-shelf packages have been proposed, the most comprehensive results in the literature are given for the ZFP compression package [Lindstrom, 2014], especially in the seismic inversion literature [Kukreja et al., 2019, Kukreja et al., 2022]. Therefore, we compare the speed, accuracy, and compression ratio of our autoencoder approach to the ZFP compression package. While the ZFP package does not require normalization, we tried both with and without normalization and found that normalizing the states before compressing was necessary

Mesh DoFs	∇ Speedup	$\mathcal{H}v$ Speedup	Relative error %
139,227,136	1.00	1.18	0.06

Table 7: Inverse results for earth-scale seismic inverse problem with higher mesh refinement, solved on 14,336 CPU cores. The gains from decompression over resolving from checkpoints for computation of the gradient is completely offset by the cost of compression. However, this cost is paid once and there is similar speedup of the Hessian-vector product as seen on a smaller problem in Table 8

to obtain accurate results. Table 8 shows the inversion results using ZFP compression for several different required accuracies. The relative errors for all methods are still quite small, but ZFP results have qualitatively different solutions than the checkpointing solution when the compression tolerance $\eta = 10^{-2}$ and $\eta = 10^{-3}$ as shown in Figure 7. Thus, $\eta \leq 10^{-4}$ is required in order to obtain comparable quality compression results to the autoencoder solution. While autoencoder compression does not show a significant advantage over ZFP in terms of speed, there is a substantial difference in the compression ratio, and hence memory footprint. With this tolerance, the compression ratio of ZFP is 8.4. On the other hand, the autoencoder compression algorithm achieved a compression ratio of 128, 15 times higher than ZFP while maintaining comparable accuracy.

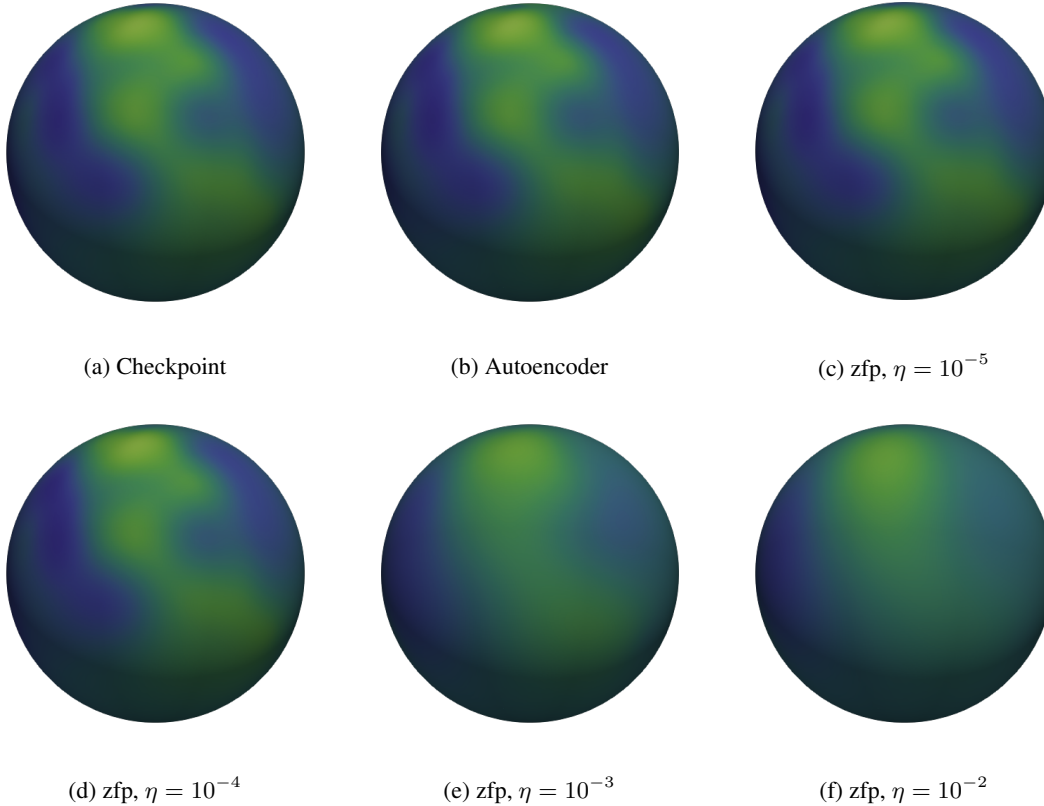


Figure 7: Comparison of inverse solutions obtained using autoencoder compression and the ZFP compression package with various compression tolerances, η . Results are shown at 130km depth on the same color scale.

4.3 DIAS regularization with autoencoder compression

As a capstone result, we show how our proposed autoencoder compression approach can be combined with the DIAS regularization [Nguyen et al., 2022] approach on the earth-scale seismic inverse problem. While the DIAS algorithm has the benefit of only applying regularization in the inactive subspace, speed is not one of its strengths. Simply estimating the active subspace for a nonlinear inverse problem requires numerous samples of the gradient — each evaluation of which requires 2 PDE solves. In the case of large-scale seismic inversion, each gradient evaluation can

Method	∇ Speedup	$\mathcal{H}v$ Speedup	Relative l_2 error %	Compression Ratio
Autoencoder	1.05	1.17	0.03	128
ZFP, $\eta = 10^{-5}$	1.0	1.09	0.004	7.2
ZFP, $\eta = 10^{-4}$	1.05	1.16	0.02	8.4
ZFP, $\eta = 10^{-3}$	1.05	1.16	0.10	11.2
ZFP, $\eta = 10^{-2}$	1.06	1.17	0.12	17.6

Table 8: Comparison of ZFP compression to autoencoder compression for various compression tolerances. There is not a significant difference in the speedup of the autoencoder compression vs the ZFP compression, but the autoencoder is able to achieve a much higher compression ratio (and hence much smaller memory footprint) while still maintaining solution accuracy. Relative l_2 error is computed with respect to the checkpoint solution.

take several minutes on dozens of compute nodes. We propose to combine the DIAS regularization algorithm with autoencoder compression to alleviate the high cost and memory footprint of checkpointing in estimating the active subspace. Since we have already discussed the speedup and memory footprint gained by the autoencoder compression at length above, we will focus on the solution quality using DIAS plus autoencoder compression in the following.

Let us briefly recap the DIAS regularization. We will focus on the DIAS-F (see [Nguyen et al., 2022, Section 4] variant, which uses the full data misfit and only applies regularization in the inactive subspace. First, the active subspace is estimated via,

$$[\mathbf{W}_1 \quad \mathbf{W}_2] \begin{bmatrix} \Lambda_1 & 0 \\ 0 & \Lambda_2 \end{bmatrix} \begin{bmatrix} \mathbf{W}_1^T \\ \mathbf{W}_2^T \end{bmatrix} = \mathbf{C} := \int \nabla_{\mathbf{u}} f(\mathbf{u}) \nabla_{\mathbf{u}} f(\mathbf{u})^T \pi_{\text{prior}}(\mathbf{u}) d\mathbf{u}, \quad (7)$$

where $f := \frac{1}{2} \|\mathcal{F}(\mathbf{u}) - \mathbf{d}\|_{\Gamma_{\text{noise}}^{-1}}^2$, \mathbf{W}_1 are the eigenvectors of \mathbf{C} corresponding to the active subspace, and \mathbf{W}_2 are the eigenvectors corresponding to the inactive subspace. As in Section 3.3.1, $\pi_{\text{prior}}(\mathbf{u})$ is the prior probability density from the Bayesian formulation of the inverse problem. The DIAS solution is then defined to be

$$\mathbf{u}_{\text{DIAS}} = \underset{\mathbf{u}}{\operatorname{argmin}} \frac{1}{2} \|\mathcal{F}(\mathbf{u}) - \mathbf{d}\|_{\Gamma_{\text{noise}}^{-1}}^2 + \frac{1}{2} \left\| \mathbf{W}_2^T (\mathbf{u} - \mathbf{u}_0) \right\|_{(\mathbf{W}_2^T \Gamma_{\text{prior}} \mathbf{W}_2)^{-1}}^2, \quad (8)$$

that is, it is a Tikhonov solution with regularization acting only on the inactive space.

For large scale problems, it is infeasible to compute and store the large matrix \mathbf{W}_2 , since the active subspace tends to be much smaller than the inactive subspace. To avoid explicitly computing and storing the potentially large matrix \mathbf{W}_2 , it can be shown using [Schott, 2016, Theorem 5.8] that

$$\left\| \mathbf{W}_2^T (\mathbf{u} - \mathbf{u}_0) \right\|_{(\mathbf{W}_2^T \Gamma_{\text{prior}} \mathbf{W}_2)^{-1}}^2 = \left\| \mathbf{P}_2 (\mathbf{u} - \mathbf{u}_0) \right\|_{(\mathbf{P}_2 \Gamma_{\text{prior}} \mathbf{P}_2)^\dagger}^2 \quad (9)$$

where $\mathbf{P}_2 := \mathbf{W}_2 \mathbf{W}_2^T = \mathcal{I} - \mathbf{W}_1 \mathbf{W}_1^T$ is a projection matrix onto the inactive subspace and $(\mathbf{P}_2 \Gamma_{\text{prior}} \mathbf{P}_2)^\dagger$ denotes the pseudoinverse.

Lest we conclude that we have a free lunch in computing the regularization term arising from the active subspace prior via \mathbf{W}_1 , there is one more challenge that remains. Note that we need to apply not the prior covariance, but its (pseudo-)inverse. That is, we need to compute $(\mathbf{P}_2 \Gamma_{\text{prior}} \mathbf{P}_2)^\dagger$. There are several factors at play here.

1. Γ_{prior} is often a sparse matrix, while $\mathbf{P}_2 \Gamma_{\text{prior}} \mathbf{P}_2$ is very likely a dense matrix.
2. We need to invert the dense matrix $\mathbf{P}_2 \Gamma_{\text{prior}} \mathbf{P}_2$ using the pseudo-inverse.
3. This matrix is in the dimension of the parameter, n .

For cases where it is feasible to form and invert $\mathbf{P}_2 \Gamma_{\text{prior}} \mathbf{P}_2$, it is also feasible to simply compute \mathbf{W}_2 explicitly. Then we can work with the lower dimensional form given in (8) which still involves inversion, but of a lower dimensional, full rank matrix. For cases where this is not feasible, we need to develop more sophisticated techniques for computing or estimating $\mathbf{P}_2 \Gamma_{\text{prior}} \mathbf{P}_2$.

The first thing one might try is to find an identity that allows us to break the projection out of the pseudo-inverse, leaving Γ_{prior} by itself. We might hope that

$$(\mathbf{P}_2 \Gamma_{\text{prior}} \mathbf{P}_2)^\dagger = \mathbf{P}_2 \Gamma_{\text{prior}}^{-1} \mathbf{P}_2,$$

but this is unfortunately not the case, as we show using Schur complements. Decompose the prior covariance as

$$\Gamma_{\text{prior}} = \begin{bmatrix} \mathbf{W}_1^T \Gamma_{\text{prior}} \mathbf{W}_1 & \mathbf{W}_1^T \Gamma_{\text{prior}} \mathbf{W}_2 \\ \mathbf{W}_2^T \Gamma_{\text{prior}} \mathbf{W}_1 & \mathbf{W}_2^T \Gamma_{\text{prior}} \mathbf{W}_2 \end{bmatrix}$$

and the inverse prior covariance as

$$\Gamma_{\text{prior}}^{-1} = \begin{bmatrix} \mathbf{W}_1^T \Gamma_{\text{prior}}^{-1} \mathbf{W}_1 & \mathbf{W}_1^T \Gamma_{\text{prior}}^{-1} \mathbf{W}_2 \\ \mathbf{W}_2^T \Gamma_{\text{prior}}^{-1} \mathbf{W}_1 & \mathbf{W}_2^T \Gamma_{\text{prior}}^{-1} \mathbf{W}_2 \end{bmatrix}.$$

Using Schur complements gives

$$\mathbf{W}_2^T \Gamma_{\text{prior}}^{-1} \mathbf{W}_2 = \left[\mathbf{W}_2^T \Gamma_{\text{prior}} \mathbf{W}_2 - \mathbf{W}_2^T \Gamma_{\text{prior}} \mathbf{W}_1 \left(\mathbf{W}_1^T \Gamma_{\text{prior}} \mathbf{W}_1 \right)^{-1} \mathbf{W}_1^T \Gamma_{\text{prior}} \mathbf{W}_2 \right]^{-1}. \quad (10)$$

While the inverse can be expanded using the Sherman-Morrison-Woodbury formula, the important observation is that the second term,

$$\mathbf{W}_2^T \Gamma_{\text{prior}} \mathbf{W}_1 \left(\mathbf{W}_1^T \Gamma_{\text{prior}} \mathbf{W}_1 \right)^{-1} \mathbf{W}_1^T \Gamma_{\text{prior}} \mathbf{W}_2$$

is not necessarily 0, except when Γ_{prior} is scaled identity. Thus, making the approximation $(\mathbf{P}_2 \Gamma_{\text{prior}} \mathbf{P}_2)^\dagger = \mathbf{P}_2 \Gamma_{\text{prior}}^{-1} \mathbf{P}_2$ incurs some error in the general case. Even though there is some error, it becomes necessary from a practical perspective to use the approximate form $\mathbf{P}_2 \Gamma_{\text{prior}}^{-1} \mathbf{P}_2$ for large scale problems.

Before the DIAS algorithm can be applied to the seismic inverse problem, we must first define an algorithm for applying DIAS to nonlinear inverse problems. One advantage of using the active subspace to define the data-informed subspace is that the active subspace is formed from the *global* average of the outer product of the gradient. This would indicate that the DIAS algorithm can be applied naively to nonlinear inverse problems:

$$\mathbf{u}_{\text{DIAS}} = \operatorname{argmin}_{\mathbf{u}} \frac{1}{2} \|\mathcal{F}(\mathbf{u}) - \mathbf{d}\|_{\Gamma_{\text{noise}}^{-1}}^2 + \frac{1}{2} \|\mathbf{P}_2(\mathbf{u} - \mathbf{u}_0)\|_{(\mathbf{P}_2 \Gamma_{\text{prior}} \mathbf{P}_2)^{-1}}^2. \quad (11)$$

However, the fact that the gradient samples are computed from draws of the prior biases the active subspace toward the directions in which the misfit function f is most sensitive near the prior mean, \mathbf{u}_0 .

Recalling that the goal of the DIAS algorithm is to remove regularization in directions that the data are more informative and that the DIAS solutions are likely closer to the usual Bayesian solution than to the prior mean for a well-chosen prior, we propose a two-step algorithm:

1. Approximately solve the usual MAP problem for \mathbf{u}_{MAP} using the full prior:

$$\mathbf{u}_{\text{MAP}} = \operatorname{argmin}_{\mathbf{u}} \frac{1}{2} \|\mathcal{F}(\mathbf{u}) - \mathbf{d}\|_{\Gamma_{\text{noise}}^{-1}}^2 + \frac{1}{2} \|\mathbf{u} - \mathbf{u}_0\|_{\Gamma_{\text{prior}}^{-1}}^2. \quad (12)$$

2. Compute the active subspace centered at \mathbf{u}_{MAP} and, with initial guess \mathbf{u}_{MAP} , solve DIAS problem:

$$\mathbf{u}_{\text{DIAS}} = \operatorname{argmin}_{\mathbf{u}} \frac{1}{2} \|\mathcal{F}(\mathbf{u}) - \mathbf{d}\|_{\Gamma_{\text{noise}}^{-1}}^2 + \frac{1}{2} \|\mathbf{P}_2(\mathbf{u} - \mathbf{u}_0)\|_{\mathbf{P}_2 \Gamma_{\text{prior}}^{-1} \mathbf{P}_2}^2.$$

Even with acceleration via autoencoder compression, the cost of gradient evaluations is still high so we estimate the active subspace using 30 gradient samples and take the active subspace to have dimension 5. The difference between the DIAS and the MAP estimate are small in this case. Compared to the true solution, the MAP estimate has average relative error of 0.3293% while the DIAS refined solution has average relative error of 0.3291%. This is reflected visually in Figure 8.

5 Conclusions

In this paper, we proposed an autoencoder compression algorithm to mitigate the high storage requirements for solving large-scale time-dependent PDE constrained inverse problems. We show the feasibility and scalability of this approach

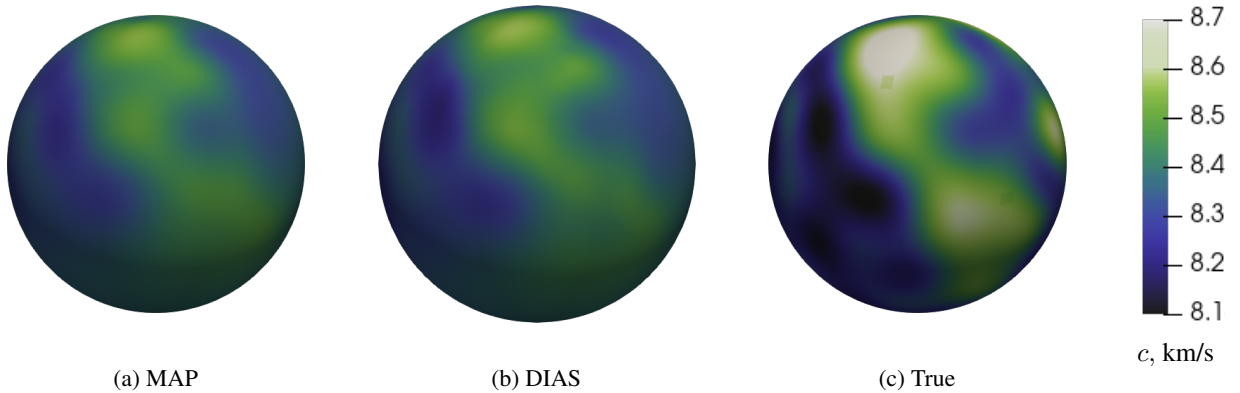


Figure 8: The DIAS solution does not differ noticeably from the MAP solution for the seismic inverse problem. Results shown for mesh with 11,166,784 DoFs.

against the popular checkpointing strategy for a seismic inverse problem on both a simple box domain with uniform refinement and a complex spherical domain with adaptive mesh refinement and a nonconforming mesh. In order to effectively train the autoencoder, we present a data generation procedure based on the Bayesian formulation that provides a problem-focused data generation scheme. We proposed two separate autoencoder compression algorithms for spatial and temporal domains. The scalability of each algorithm was shown, providing a clear close-to-ideal speed advantage on large scale problems compared to the traditional checkpointing approach and a substantial improvement in the compression ratio of the state-of-the-art floating point compression package, ZFP. While there are clear advantages of using autoencoders to perform compression, care must be taken in their implementation in order for there to be an advantage over the checkpointing approach. As an important application of the proposed autoencoder algorithm, we combined the proposed autoencoder compression approach with the DIAS prior to show how the DIAS method can be affordably extended to large scale problems without the need of checkpointing and large memory.

6 Acknowledgements

We would like to thank Georg Stadler for his many correspondences and helpful advice on stably solving the forward and inverse problem in large scale runs; Jau-Uei Chen for sharing his insight on the discontinuous Galerkin method; Sheroze Sherifdeen and Hwan Goh for their many discussions on autoencoders, compression, and HPC; and the Texas Advanced Computing Center (TACC) at the University of Texas at Austin for providing HPC resources that contributed to the results presented in this work. URL: <http://www.tacc.utexas.edu>. This research is partially funded by the National Science Foundation awards NSF-OAC-2212442, NSF-2108320, NSF-1808576 and NSF-CAREER-1845799; and by the Department of Energy awards DE-SC0018147 and DE-SC0022211.

References

- [int,] Intel® xeon® platinum 8280 processor (38.5m cache, 2.70 ghz) - product specifications.
- [Abu Alsheikh et al., 2014] Abu Alsheikh, M., Poh, P. K., Lin, S., Tan, H.-P., and Niyato, D. (2014). Efficient data compression with error bound guarantee in wireless sensor networks. In *Proceedings of the 17th ACM international conference on Modeling, analysis and simulation of wireless and mobile systems*, pages 307–311.
- [Akturk and Karpuzcu, 2018] Akturk, I. and Karpuzcu, U. R. (2018). Trading computation for communication: A taxonomy of data recomputation techniques. *IEEE Transactions on Emerging Topics in Computing*, 9(1):496–506.
- [Baldi and Hornik, 1989] Baldi, P. and Hornik, K. (1989). Neural networks and principal component analysis: Learning from examples without local minima. *Neural networks*, 2(1):53–58.
- [Bharadwaj et al., 2021] Bharadwaj, K. K., Srivastava, A., Panda, M. K., Singh, Y. D., Maharana, R., Mandal, K., Singh, M., Singh, D., Das, M., Murmu, D., et al. (2021). Computational intelligence in vaccine design against covid-19. In *Computational intelligence methods in COVID-19: surveillance, prevention, prediction and diagnosis*, pages 311–329. Springer.
- [Bhattacharjee and Wells, 2021] Bhattacharjee, A. and Wells, J. (2021). Preface to special topic: Building the bridge to the exascale—applications and opportunities for plasma physics.

- [Bickelhaupt and Baerends, 2000] Bickelhaupt, F. M. and Baerends, E. J. (2000). Kohn-sham density functional theory: predicting and understanding chemistry. *Reviews in computational chemistry*, pages 1–86.
- [Bjerge et al., 2022] Bjerge, K., Mann, H. M., and Høyve, T. T. (2022). Real-time insect tracking and monitoring with computer vision and deep learning. *Remote Sensing in Ecology and Conservation*, 8(3):315–327.
- [Blessner, 1969] Blessner, B. (1969). Audio dynamic range compression for minimum perceived distortion. *IEEE Transactions on Audio and Electroacoustics*, 17(1):22–32.
- [Boehm et al., 2016] Boehm, C., Hanzich, M., de la Puente, J., and Fichtner, A. (2016). Wavefield compression for adjoint methods in full-waveform inversion. *Geophysics*, 81(6):R385–R397.
- [Bui-Thanh et al., 2012] Bui-Thanh, T., Burstedde, C., Ghattas, O., Martin, J., Stadler, G., and Wilcox, L. C. (2012). Extreme-scale uq for bayesian inverse problems governed by pdes. In *SC’12: Proceedings of the international conference on high performance computing, networking, storage and analysis*, pages 1–11. IEEE.
- [Bui-Thanh et al., 2013] Bui-Thanh, T., Ghattas, O., Martin, J., and Stadler, G. (2013). A computational framework for infinite-dimensional bayesian inverse problems part i: The linearized case, with application to global seismic inversion. *SIAM Journal on Scientific Computing*, 35(6):A2494–A2523.
- [Bukowski et al., 2010] Bukowski, R., Sun, Q., Howard, M., and Pillardy, J. (2010). Biohpc: computational biology application suite for high performance computing. *Journal of Biomolecular Techniques: JBT*, 21(3 Suppl):S23.
- [Cheng et al., 2018] Cheng, Z., Sun, H., Takeuchi, M., and Katto, J. (2018). Deep convolutional autoencoder-based lossy image compression. In *2018 Picture Coding Symposium (PCS)*, pages 253–257. IEEE.
- [Cyr et al., 2015] Cyr, E. C., Shadid, J., and Wildey, T. (2015). Towards efficient backward-in-time adjoint computations using data compression techniques. *Computer Methods in Applied Mechanics and Engineering*, 288:24–44.
- [De Jong et al., 2010] De Jong, W. A., Bylaska, E., Govind, N., Janssen, C. L., Kowalski, K., Müller, T., Nielsen, I. M., van Dam, H. J., Veryazov, V., and Lindh, R. (2010). Utilizing high performance computing for chemistry: parallel computational chemistry. *Physical Chemistry Chemical Physics*, 12(26):6896–6920.
- [Denis et al., 2022] Denis, A., Jeannot, E., and Swartvagher, P. (2022). Modeling memory contention between communications and computations in distributed hpc systems. In *IPDPS-2022-IEEE International Parallel and Distributed Processing Symposium Workshops*, page 10.
- [Dillon et al., 2021] Dillon, B., Plehn, T., Sauer, C., and Sorrenson, P. (2021). Better latent spaces for better autoencoders. *SciPost Physics*, 11(3):061.
- [Doi et al., 2019] Doi, J., Takahashi, H., Raymond, R., Imamichi, T., and Horii, H. (2019). Quantum computing simulator on a heterogenous hpc system. In *Proceedings of the 16th ACM International Conference on Computing Frontiers*, pages 85–93.
- [Duarte et al., 2020] Duarte, E. F., da Costa, C. A., de Araújo, J. M., Wang, Y., and Rao, Y. (2020). Seismic shot-encoding schemes for waveform inversion. *Journal of Geophysics and Engineering*, 17(5):906–913.
- [Epanomeritakis et al., 2008] Epanomeritakis, I., Akçelik, V., Ghattas, O., and Bielak, J. (2008). A newton-cg method for large-scale three-dimensional elastic full-waveform seismic inversion. *Inverse Problems*, 24(3):034015.
- [Esteva et al., 2021] Esteva, A., Chou, K., Yeung, S., Naik, N., Madani, A., Mottaghi, A., Liu, Y., Topol, E., Dean, J., and Socher, R. (2021). Deep learning-enabled medical computer vision. *NPJ digital medicine*, 4(1):1–9.
- [Fedeli et al., 2022] Fedeli, L., Huebl, A., Boillod-Cerneux, F., Clark, T., Gott, K., Hillairet, C., Jaure, S., Leblanc, A., Lehe, R., Myers, A., et al. (2022). Pushing the frontier in the design of laser-based electron accelerators with groundbreaking mesh-refined particle-in-cell simulations on exascale-class supercomputers. In *2022 SC22: International Conference for High Performance Computing, Networking, Storage and Analysis (SC)*, pages 25–36. IEEE Computer Society.
- [Fichtner et al., 2006] Fichtner, A., Bunge, H.-P., and Igel, H. (2006). The adjoint method in seismology: I. theory. *Physics of the Earth and Planetary Interiors*, 157(1-2):86–104.
- [Ge et al., 2013] Ge, H., Wang, Y., Li, C., Chen, N., Xie, Y., Xu, M., He, Y., Gu, X., Wu, R., Gu, Q., et al. (2013). Molecular dynamics-based virtual screening: accelerating the drug discovery process by high-performance computing. *Journal of chemical information and modeling*, 53(10):2757–2764.
- [Giles and Pierce, 2000] Giles, M. B. and Pierce, N. A. (2000). An introduction to the adjoint approach to design. *Flow, turbulence and combustion*, 65(3):393–415.
- [Goh et al., 2019] Goh, H., Sherifdeen, S., Wittmer, J., and Bui-Thanh, T. (2019). Solving bayesian inverse problems via variational autoencoders. *arXiv preprint arXiv:1912.04212*.

- [Griewank and Walther, 1997] Griewank, A. and Walther, A. (1997). Treeverse: An implementation of checkpointing for the reverse or adjoint mode of computational differentiation. *Preprint IOKOMO-04-1997, Technische Universitat, Dresden*.
- [Habashy et al., 2011] Habashy, T., Abubakar, A., Pan, G., and Belani, A. (2011). Source-receiver compression scheme for full-waveform seismic inversion. *Geophysics*, 76(4):R95–R108.
- [Hinton and Salakhutdinov, 2006] Hinton, G. E. and Salakhutdinov, R. R. (2006). Reducing the dimensionality of data with neural networks. *science*, 313(5786):504–507.
- [Imani et al., 2019] Imani, M., Gupta, S., Kim, Y., Zhou, M., and Rosing, T. (2019). Digitalpim: Digital-based processing in-memory for big data acceleration. In *Proceedings of the 2019 on Great Lakes Symposium on VLSI*, pages 429–434.
- [Ji et al., 2012] Ji, S., Xu, W., Yang, M., and Yu, K. (2012). 3d convolutional neural networks for human action recognition. *IEEE transactions on pattern analysis and machine intelligence*, 35(1):221–231.
- [Kaipio and Somersalo, 2006] Kaipio, J. and Somersalo, E. (2006). *Statistical and computational inverse problems*, volume 160. Springer Science & Business Media.
- [Kamath et al., 2019] Kamath, U., Liu, J., and Whitaker, J. (2019). *Deep learning for NLP and speech recognition*, volume 84. Springer.
- [Kates-Harbeck et al., 2019] Kates-Harbeck, J., Svyatkovskiy, A., and Tang, W. (2019). Predicting disruptive instabilities in controlled fusion plasmas through deep learning. *Nature*, 568(7753):526–531.
- [Kaur and Choudhary, 2016] Kaur, R. and Choudhary, P. (2016). A review of image compression techniques. *Int. J. Comput. Appl*, 142(1):8–11.
- [Kingma and Welling, 2013] Kingma, D. P. and Welling, M. (2013). Auto-encoding variational bayes. *arXiv preprint arXiv:1312.6114*.
- [Kneer et al., 2021] Kneer, S., Sayadi, T., Sipp, D., Schmid, P., and Rigas, G. (2021). Symmetry-aware autoencoders: s-pca and s-nlpc. *arXiv preprint arXiv:2111.02893*.
- [Kowalski et al., 2021] Kowalski, K., Bair, R., Bauman, N. P., Boschen, J. S., Bylaska, E. J., Daily, J., de Jong, W. A., Dunning Jr, T., Govind, N., Harrison, R. J., et al. (2021). From nwchem to nwchemex: Evolving with the computational chemistry landscape. *Chemical reviews*, 121(8):4962–4998.
- [Kukreja et al., 2019] Kukreja, N., Hüchelheim, J., Louboutin, M., Hovland, P., and Gorman, G. (2019). Combining checkpointing and data compression to accelerate adjoint-based optimization problems. In *European Conference on Parallel Processing*, pages 87–100. Springer.
- [Kukreja et al., 2022] Kukreja, N., Hüchelheim, J., Louboutin, M., Washbourne, J., Kelly, P. H., and Gorman, G. J. (2022). Lossy checkpoint compression in full waveform inversion: a case study with zfpv0. 5.5 and the overthrust model. *Geoscientific Model Development*, 15(9):3815–3829.
- [Ladjal et al., 2019] Ladjal, S., Newson, A., and Pham, C.-H. (2019). A pca-like autoencoder. *arXiv preprint arXiv:1904.01277*.
- [Lee et al., 2022] Lee, J., Gong, Q., Choi, J., Banerjee, T., Klasky, S., Ranka, S., and Rangarajan, A. (2022). Error-bounded learned scientific data compression with preservation of derived quantities. *Applied Sciences*, 12(13):6718.
- [Lewis and Knowles, 1990] Lewis, A. and Knowles, G. (1990). Video compression using 3d wavelet transforms. *Electronics Letters*, 26(6):396–398.
- [Lindstrom, 2014] Lindstrom, P. (2014). Fixed-rate compressed floating-point arrays. *IEEE transactions on visualization and computer graphics*, 20(12):2674–2683.
- [Liu et al., 2021a] Liu, J., Di, S., Zhao, K., Jin, S., Tao, D., Liang, X., Chen, Z., and Cappello, F. (2021a). Exploring autoencoder-based error-bounded compression for scientific data. In *2021 IEEE International Conference on Cluster Computing (CLUSTER)*, pages 294–306. IEEE.
- [Liu et al., 2021b] Liu, T., Wang, J., Liu, Q., Alibhai, S., Lu, T., and He, X. (2021b). High-ratio lossy compression: Exploring the autoencoder to compress scientific data. *IEEE Transactions on Big Data*.
- [Liu et al., 2021c] Liu, Y., Liu, X., Li, F., Fu, H., Yang, Y., Song, J., Zhao, P., Wang, Z., Peng, D., Chen, H., et al. (2021c). Closing the "quantum supremacy" gap: achieving real-time simulation of a random quantum circuit using a new sunway supercomputer. In *Proceedings of the International Conference for High Performance Computing, Networking, Storage and Analysis*, pages 1–12.

- [Mandrà et al., 2021] Mandrà, S., Marshall, J., Rieffel, E. G., and Biswas, R. (2021). Hybridq: A hybrid simulator for quantum circuits. In *2021 IEEE/ACM Second International Workshop on Quantum Computing Software (QCS)*, pages 99–109. IEEE.
- [McFarlane and Biktasheva, 2008] McFarlane, R. and Biktasheva, I. V. (2008). Beatbox—a computer simulation environment for computational biology of the heart. In *Visions of Computer Science—BCS International Academic Conference*, pages 99–109. British Computer Society.
- [Nadeau and Bengio, 1999] Nadeau, C. and Bengio, Y. (1999). Inference for the generalization error. *Advances in neural information processing systems*, 12.
- [Nguyen et al., 2022] Nguyen, H., Wittmer, J., and Bui-Thanh, T. (2022). Dias: A data-informed active subspace regularization framework for inverse problems. *Computation*, 10(3):38.
- [Peng et al., 2020] Peng, I., Wu, K., Ren, J., Li, D., and Gokhale, M. (2020). Demystifying the performance of hpc scientific applications on nvm-based memory systems. In *2020 IEEE International Parallel and Distributed Processing Symposium (IPDPS)*, pages 916–925. IEEE.
- [Plaut, 2018] Plaut, E. (2018). From principal subspaces to principal components with linear autoencoders. *arXiv preprint arXiv:1804.10253*.
- [Quarteroni et al., 2010] Quarteroni, A., Sacco, R., and Saleri, F. (2010). *Numerical mathematics*, volume 37. Springer Science & Business Media.
- [Reichstein et al., 2019] Reichstein, M., Camps-Valls, G., Stevens, B., Jung, M., Denzler, J., Carvalhais, N., et al. (2019). Deep learning and process understanding for data-driven earth system science. *Nature*, 566(7743):195–204.
- [Scales and Tenorio, 2001] Scales, J. A. and Tenorio, L. (2001). Prior information and uncertainty in inverse problems. *Geophysics*, 66(2):389–397.
- [Schmidt and Hildebrandt, 2017] Schmidt, B. and Hildebrandt, A. (2017). Next-generation sequencing: big data meets high performance computing. *Drug discovery today*, 22(4):712–717.
- [Schott, 2016] Schott, J. R. (2016). *Matrix analysis for statistics*. John Wiley & Sons.
- [Stanzione et al., 2020] Stanzione, D., West, J., Evans, R. T., Minyard, T., Ghattas, O., and Panda, D. K. (2020). Frontera: The evolution of leadership computing at the national science foundation. In *Practice and Experience in Advanced Research Computing*, pages 106–111.
- [Sukumar et al., 2021] Sukumar, S. R., Balma, J. A., Rickett, C. D., Maschhoff, K. J., Landman, J., Yates, C. R., Chittiboyina, A. G., Peterson, Y. K., Vose, A., Byler, K., et al. (2021). The convergence of hpc, ai and big data in rapid-response to the covid-19 pandemic. In *Smoky Mountains Computational Sciences and Engineering Conference*, pages 157–172. Springer.
- [Usevitch, 2001] Usevitch, B. E. (2001). A tutorial on modern lossy wavelet image compression: foundations of jpeg 2000. *IEEE signal processing magazine*, 18(5):22–35.
- [Wang et al., 2009] Wang, Q., Moin, P., and Iaccarino, G. (2009). Minimal repetition dynamic checkpointing algorithm for unsteady adjoint calculation. *SIAM Journal on Scientific Computing*, 31(4):2549–2567.
- [Wilcox et al., 2015] Wilcox, L. C., Stadler, G., Bui-Thanh, T., and Ghattas, O. (2015). Discretely exact derivatives for hyperbolic pde-constrained optimization problems discretized by the discontinuous galerkin method. *Journal of Scientific Computing*, 63(1):138–162.
- [Wu et al., 2017] Wu, K., Ober, F., Hamlin, S., and Li, D. (2017). Early evaluation of intel optane non-volatile memory with hpc i/o workloads. *arXiv preprint arXiv:1708.02199*.
- [Yang, 2009] Yang, J. (2009). Newton-conjugate-gradient methods for solitary wave computations. *Journal of Computational Physics*, 228(18):7007–7024.
- [You et al., 2019] You, Y., Li, J., Reddi, S., Hseu, J., Kumar, S., Bhojanapalli, S., Song, X., Demmel, J., Keutzer, K., and Hsieh, C.-J. (2019). Large batch optimization for deep learning: Training bert in 76 minutes. *arXiv preprint arXiv:1904.00962*.
- [Zhang and Constantinescu, 2023] Zhang, H. and Constantinescu, E. M. (2023). Optimal checkpointing for adjoint multistage time-stepping schemes. *Journal of Computational Science*, 66:101913.
- [Zhao et al., 2020] Zhao, Y., Chen, X., Wang, Y., Li, C., You, H., Fu, Y., Xie, Y., Wang, Z., and Lin, Y. (2020). Smartexchange: Trading higher-cost memory storage/access for lower-cost computation. In *2020 ACM/IEEE 47th Annual International Symposium on Computer Architecture (ISCA)*, pages 954–967. IEEE.